Journal of Materials Chemistry A

PAPER

View Article Online
View Journal | View Issue

Cite this: J. Mater. Chem. A, 2018, 6, 1531

Diffusion and selectivity of water confined within metal–organic nanotubes.†

Ashini S. Jayasinghe, Maurice K. Payne, Daniel K. Unruh, Adam Johns, Johna Leddy * and Tori Z. Forbes *

Received 31st July 2017
Accepted 18th December 2017

DOI: 10.1039/c7ta06741k

rsc.li/materials-a

Behavior of nanoconfined water in porous materials has important implications for the development of advanced water purification and storage. In the current study, the kinetics of water sorption from the vapor phase into a metal organic nanotube ($(C_4N_2H_6)[(UO_2)(C_4O_4NH_5)(C_4O_4NH_6)]\cdot 2H_2O$ (UMON)) are investigated with varying relative humidity. The UMON compound contains nanoconfined water molecules arranged in an ice-like array along the length of its one-dimensional pore and exhibits complete specificity to liquid water. Total hydration of the material is observed upon exposure to relative humidity of 60% or higher. Water uptake curves are modeled as diffusion and irreversible condensation in the pore, which leads to a modeled diffusion coefficient of $(1.2 \pm 0.6) \times 10^{-12}$ cm^2 s^{-1} for water in UMON nanochannels. This value is much lower than observed for other porous material and is most similar to water diffusivity in low-density amorphous ice. In addition, on exposure to various solvent vapors, the UMON material maintained specificity for water in the gas phase.

Introduction

The chemistry of water confined within nanopores is of interest to diverse scientific communities because of its unique behavior and applications in materials, transport systems, and separations. Interdisciplinary discussions on nanoconfined water began as early as 1948 with Faraday Society meetings[1] and initial studies focused on both soft (micelles,[2–5] polymer matrices[6–8]) and hard (zeolites,[9–11] clays[12–15]) materials. More recently, advancements in nanotechnology have led to the controlled synthesis of carbon nanotubes,[16,17] lipid layers,[18–20] and porous hybrid materials (*i.e.*, metal organic frameworks)[21] that provide varied surface chemistries for interaction with water molecules within confined environments.

Detailed experimental and computational investigations of these materials demonstrate water molecules behave differently under nanoconfinement than in bulk solution.[22–26] Single-walled carbon nanotubes are one of the most well-studied systems, where surprisingly, water will spontaneously fill hydrophobic nanotubes when the pore diameter is between 0.8 to 2.0 nm.[27] Other unusual properties of water confined in carbon nanotubes include rapid fluid transport rates,[28] increased proton conduction,[29,30] superpermittivity,[31] and decreased liquid–solid transition temperature that drives the formation of a multitude of ice-like structures with varied hydrogen bonding motifs.[32] Understanding these divergent properties is important for the development of novel technologies related to energy and sustainability, including nanofluidics, artificial biomembranes, water purification/capture, heat storage, and thermal adsorption batteries. Important aspects for continued advancement in these areas are the quantitative assessment of the water sorption capabilities and specificity in a wide range of materials.

We have previously developed a hybrid metal organic nanotube, $(pip)_{0.5}[(UO_2)(HIDA)(H_2IDA)]\cdot 2H_2O$ (pip = piperazinium; IDA = iminodiacetate) (UMON), that contains nanoconfined water molecules and exhibits unusual water uptake and transport behavior (Fig. 1).[33] Similar to carbon nanotubes,[27,32,34] we observed an ordered array of water molecules that was characterized by single-crystal X-ray diffraction. Structural analysis of this material indicated that there were two crystallographically unique water molecules (OW1 and OW2) located inside the nanoscale channels that are arranged in a well-ordered hexameric array with similarities to ice.[33] Unlike carbon nanotubes, the ice-like array persists at room temperature with reversible dehydration at 37 °C. Quantitative measurements, such as the rate of water uptake and the diffusion coefficient of water inside the pore space, are necessary to provide insight into the unusual water ordering and structure. This compound is also unusual because it is specific to water over common solvents, even when immersed in liquid solvents for up to 16 hours.[33,35] Additional studies are also necessary to determine if the same selectivity observed for liquid water would extend to vapor phase solvents.

Department of Chemistry, University of Iowa, Iowa City, IA 52242, USA. E-mail: johna-leddy@uiowa.edu; tori-forbes@uiowa.edu

† Electronic supplementary information (ESI) available: Modeling details, experimental fitting parameters, FTIR of evolved gases, powder XRD. See DOI: 10.1039/c7ta06741k

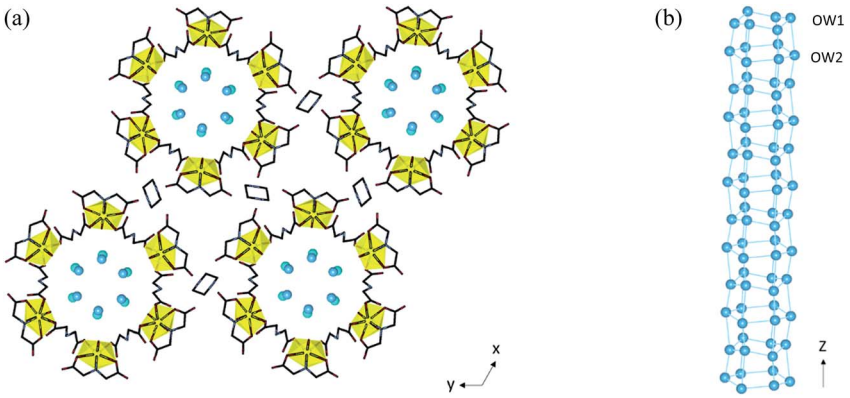

Fig. 1 (a) Structural features of the UMON material include uranyl pentagonal bipyramids (yellow polyhedra) that are linked through iminodiacetate ligands to form the nanotubular units. Piperazinium cations are located between the nanotubes. Water molecules (blue spheres) are found in an ordered array within the 1-D pores. (b) The water molecules (OW1 and OW2) form a hydrogen bonding network along the length of the tube that has structural features with similarities to bulk ice.

Herein, we quantitatively characterized water uptake in UMON material and determined diffusion coefficients (D) by fitting an analytical expression (derived in the ESI†) that characterizes time dependent water transport into the nanochannels. In addition, we extended our previous work[35] to investigate uptake of non-aqueous solvent vapors, specifically focusing on molecules with a wide range of polarities, shapes, and sizes to further investigate the selectivity of the UMON nanotube. These results have also been discussed in the context of other porous material, with specific emphasis on the well-studied family of metal organic frameworks (MOFs), to highlight the unique nature of the confined water within the UMON material.

Experimental methods

Synthesis of UMON material

All solutions were prepared using Millipore water (18.2 MΩ cm), and chemicals purchased were used without further purification. Iminodiacetate and piperazine were purchased from Alfa Aesar, whereas the uranyl nitrate hexahydrate was bought from Flynn Scientific, Inc. *CAUTION: $(UO_2)(NO_3)_2{\cdot}6H_2O$ contains radioactive ^{238}U, which is an α emitter, and like all radioactive materials must be handled with care. These experiments were conducted by trained personnel in a licensed research facility with special precautions taken toward the handling, monitoring, and disposal of radioactive materials.*

Stock solutions of 0.2 M uranyl nitrate hexahydrate, iminodiacetate, and piperazine were prepared in water. Equal amounts of iminodiacetic acid (3 mL, 0.6 mmol) and piperazine (3 mL, 0.6 mmol) stock solutions were mixed with 1.5 mL of uranyl nitrate hexahydrate (3 mL, 0.3 mmol) in a glass scintillation vial. Acetone (7.0 mL) was carefully added to the aqueous solution and after three to five days, large (100–1000 μm), columnar, yellow crystals formed on the bottom of the vial with yields of 95% based upon U. These crystals were filtered, washed with acetone, and dried under ambient conditions. Powder X-ray diffraction was used to confirm the purity of the sample.

Water vapor sorption experiments

Water sorption into the UMON materials was measured with a custom built vapor sorption apparatus (Fig. 2). UMON crystals were ground into a polycrystalline powder, dehydrated at 80 °C for 24 hours, placed into the chamber, and the dry weight of the initial sample was recorded at room temperature using a METTLER AT20 microbalance. Dry air was bubbled through a sealed chamber containing 300 mL of ultrapure water and then the relative humidity was controlled by combining the saturated air with a secondary stream of dry air. Relatively humidity of the sample chamber was maintained at 30%, 45%, 60%, and 80% (±2%) and a flow meter was used to control the volume of vapor passed over the UMON in the sample chamber. Water uptake was monitored by measuring the weight change of the sample every 15 minutes for a total experimental time of 90 minutes. Samples were run in triplicate for each relative humidity using fresh material for each experiment. In the case of the 45% and 30% relative humidity experiments, the time was extended to 360 minutes and 600 minutes, respectively, to ensure that the total uptake within this environment was assessed adequately.

Initial estimates of water uptake rates in the UMON material were calculated by assuming that the weight increase in the UMON is solely due to the addition of water mass to the sample, with observed weight changes converted into total moles of water. The theoretical density (2.084 g cm^{-3}) of the UMON material was determined from the previous structural characterization of the material. CrystalMaker (version 2.5.0) was used to determine the pore volume per unit cell (ε = 0.9732) and pore diameter (1.2 nm to yield pore radius r of 0.6 nm) of the UMON nanotube. The pore length l was determined by collecting scanning electron microscopy images (Hitachi S-3400 N) of the ground material and using ImageJ software[36] to measure the length of 220 crystallites. The particle size distribution was plotted *versus* the log size (Fig. SI.9†) and a size of 2 μm was chosen for l based upon the mode.

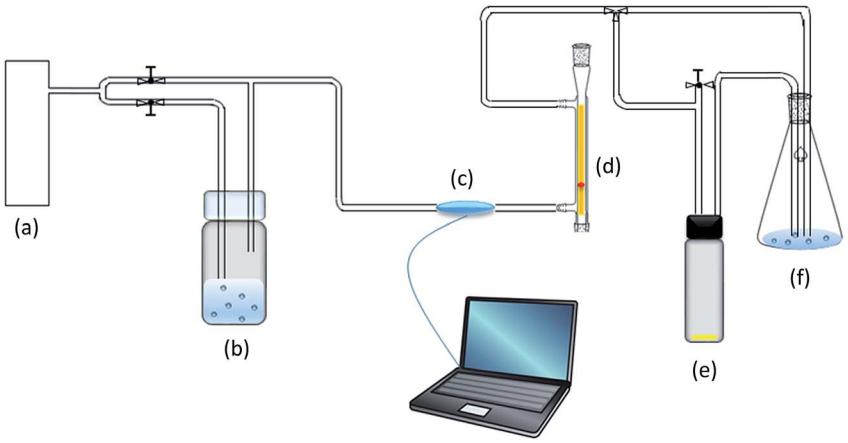

Fig. 2 Vapor sorption apparatus includes (a) dry air source, (b) water chamber, (c) relative humidity sensor, (d) flow meter, (e) sample chamber, and (f) overflow chamber.

Water sorption model

The model describes a space x (cm) and time t (s) dependent concentration $c(x,t)$ for diffusing species in a nanochannel. The nanochannel is characterized by a length l (cm) where the pore radius (cm) $r \ll l$ and a one dimensional model suffices. Motion of diffusing species is specified by Fick's second law and a diffusion coefficient in the nanochannel, D. Initially, no species has diffused into the pore and $c(x,0) = 0$. The concentration at outer edges of the pore, where $x = 0$ and $x = l$, are set by the concentration in the vapor, c^* (g cm^{-3}) that is calculated from the relative humidity RH of the vapor. Once in the pore, diffusing species undergoes irreversible, first order transformation at frequency k (s^{-1}).

An analytical expression for the diffusing species into the channel is found for

$$\frac{\partial c(x,t)}{\partial t} = D\frac{\partial^2 c(x,t)}{\partial x^2} - kc(x,t) \quad (1)$$

by Laplace transforms. The solution $c(x,t)$ is set by the sum of several infinite series of exponential error functions that are evaluated in Excel. The weight accumulated in the nanochannel as a function of time $w(t)$ is found by integrating $c(x,t)$ with respect to x and with respect to t.

The model variables are described by dimensionless parameters β and τ.

$$\beta = \frac{l\sqrt{k}}{\sqrt{D}} \quad (2)$$

$$\tau = \sqrt{kt} \quad (3)$$

β expresses the ratio of rates for the following reaction to the transport in the channel. When β is approximately 1, these two rates are comparable. The dimensionless time is captured in τ^2. At saturation, the weight of water in the pore reaches equilibrium, $w_{eq.}$.

$$w(t\rightarrow\infty) = w_{eq.} = 2\pi r^2 lN\frac{l}{r}c^*\frac{2}{\beta}\tanh\left[\frac{\beta}{2}\right] \quad (4)$$

$$w_{eq.} = 2\varepsilon\frac{l}{r}c^*\frac{2}{\beta}\tanh\left[\frac{\beta}{2}\right] \quad (5)$$

Porosity of the particles ε is in cm^3 g^{-1}. The number of nanochannels per gram is N. The model development is detailed further in the ESI.†

From the model, gas enters the pore and condenses or is otherwise lost from the gas phase at a frequency k. The dimensionless weight in the gas phase $f(x,t)$ and condensate $w(t)$ are interdependent through β. For β in the range of 0.1 to 20, the rates of transport and condensation are comparable and may be assessed experimentally. The behavior of gas and condensate in the pore are detailed in Fig. SI.3 and SI.5–SI.7. † The equilibrium $w_{eq.}$ as a function of β is shown in Fig. SI.4. † The time evolution $w(t)$ with $\log\tau^2 = \log k + \log t$ for various values of β is mapped in Fig. SI.8. † Model values of $w(kt)$ with kt are tabulated in Fig. SI.14 and SI.15. †

Modeling fitting procedure

Data from the water vapor sorption experiments are plotted for 30, 45, 60, and 80% relative humidity as the experimental, dimensionless weight recorded with time $w(t)$, where $w(t)$ is weight of sorbed water per weight of dry particles (Fig. SI.10–SI.13†). At saturation, equilibrium is reached and denoted as $w_{eq.}$. The expression for $w_{eq.}$ in eqn (4) and (5) includes a normalization $c^*\varepsilon l/r$, where c^* is calculated from relative humidity RH (Section SI.6.1, c^*(g cm^{-3}) = 2.30 × 10^{-7} RH (%) at 25 °C). Measureable parameters (*vide supra*) needed to fit the data are r (6 × 10^{-8} cm), l (2 μm), and ε (0.9732). Because $\varepsilon = N\pi r^2 l$, $N = \varepsilon/[\pi r^2 l] = 4.3 \times 10^{17}$ pores per gram.

For plots of $w(t)$ *versus* $\log t$ for all relative humidity values found in Fig. SI.10–SI.13, † data were fit systematically to the model with the exception of the 30% relative humidity level as insufficient water was sorbed for that sample to allow reliable measurement. Samples at 30% RH will not be considered for the model. As above, data are normalized by $2c^*\varepsilon l/r$ and the value at 90 minutes is taken as equilibrium such that:

$$\frac{w_{eq.}}{2c^{*}\varepsilon l/r} = \frac{2}{\beta}\tanh\frac{\beta}{2} \quad (6)$$

For $x = \beta/2$, successive optimization of x in the model yields the value of β that fits the experimentally determined $w_{eq.}$. The value of β is then used to fit the time dependence and τ^2 is found. Given β, τ^2, and l, D ($cm^2\ s^{-1}$) and k are found. The details of the fitting process and some statistics (Tables SI.2 to SI.4†) are outlined in the ESI.†

Non-aqueous solvent vapor uptake experiments

A subsample (30 mg) of the characterized UMON crystals were placed into separate vials and heated at 110 °C for 24 hours to dehydrate the material. While at temperature, the samples were removed from the oven and the vials were placed in a secondary vessel (20 mL scintillation vial) that contained 3.00 mL of the solvent. The secondary container was capped to create a saturated environment within the chamber. Non-aqueous vapor sorption of the UMON crystals was explored using a range of common solvents with different polarities, sizes, and shapes (acetone, methanol, ethanol, 1-propanol, 2-propanol, 1-butanol, 1-pentanol, pentane, cyclopentane, hexane, cyclohexane, THF, benzene, toluene, 1,4-dioxane, and NH_3). The samples were kept in the saturated chamber for 16 hours, immediately loaded onto an aluminum TGA pan, placed on the TAQ500 thermogravimetric analyzer, and heated to 180 °C at the ramp rate of 20 °C per minute. Gasses released during the heat cycle were passed through a transfer line that was stabilized at 225 °C and analyzed with a Nicolet 4700 Fourier transform infrared spectrometer. For the NH_3 uptake experiments, it was necessary to monitor the experiment for material degradation; thus, a 200 mg sample of the UMON crystals were placed into a glass vial saturated with gaseous NH_3 and subsamples were analyzed using PXRD at different time intervals up to 48 hours. Diffractograms were collected from 5 to 60° 2θ with a step size of 0.02° 2θ and a count time of 1 s per step on a Bruker D-8 ADVANCE diffractometer equipped with Cu Kα radiation and a LynxEye solid state detector.

Structural characterization

Single crystal X-ray diffraction was also used when highly crystalline material was present as a degradation product (NH_3 uptake experiment) and to additionally characterize the partially hydrated UMON material. High-quality single crystals were isolated, coated in oil, and mounted on a Nonius Quest CCD single-crystal X-ray diffractometer equipped with Mo Kα radiation ($\lambda = 0.7107$ Å) and a low-temperature cryostat. Data were collected at 100 K with the Nonius Collect software package[37] and peak intensities were corrected for Lorentz, polarization, and background effects using Bruker APEX II software.[38] An empirical absorption correction was applied with the program SADABS[39] and the structure solution was determined by intrinsic phasing methods and refined on the basis of F^2 for all unique data using the SHELXTL version 5 series of programs.[40] U atoms were located by direct methods and the O, N, and C atom positions were identified in the difference Fourier maps calculated following refinement of the partial-structure models. Hydrogen atom positions associated with water molecules were found in the difference map and refined by applying restraints with temperature appropriate distances and angles. H-atoms connected to the organic linkers were fixed using a riding model.

Results and discussion

Water uptake rates at different relative humidity levels

As the relative humidity in the chamber increases, complete hydration is achieved and the time to reach steady state decreases (Fig. 3). At 80% and 60% relative humidity, the UMON material is completely hydrated as indicated by the same equilibrium weight ($w_{eq.}$) gain of 5.5% (2 moles of H_2O per mole U). The time to reach full hydration changes with the relative humidity of the sample chamber and saturation occurs after 45 and 75 minutes for 80% and 60%, respectively. At the lower relative humidity values of 45% and 30%, equilibrium water sorption is decreased, with only 3% (1.2 moles H_2O per mole of U) and 1% (0.37 moles H_2O per mole of U) weight gain, respectively. Equilibrium for the 45% relative humidity samples occurs at 180 minutes, where the weight gain plateaus at 4.8 weight% (1.74 mole H_2O per mole U) (Fig. SI.12†). At 30% relative humidity, water sorption measured at 15 minutes intervals remained unchanged across the total collection time of 600 minutes (Fig. SI.13†). This partial hydration supports our previously reported qualitative data.[41]

Only a handful of well-characterized metal organic nanotubular compounds have been reported in the literature;[42] thus, we turn to the vast literature on metal organic frameworks to place the sorption isotherms for the UMON sample in perspective. Metal organic frameworks are hybrid materials with high pore volume[43,44] that can be utilized in some cases for

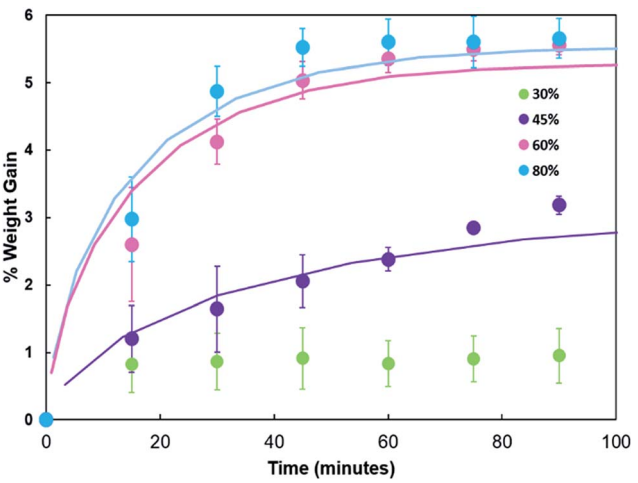

Fig. 3 Water uptake (% weight gain) *versus* time (s) at four relative humidity levels (30%, 45%, 60%, and 80%) for the UMON material. Solid lines are the fit of the model to the data based on parameters outlined in Table 2 and an equilibrium weight at 90 minutes.

water sorption.[45–48] Several MOFs, including MIL-100, MIL-101, MIL-53, Ni-CPO-27(MOF-74) and HKUST-1 have been identified as potential candidates for water sorption applications due to their stability in humid environments and their water sorption capacity, at 0.81, 1.28, 0.10, 0.68, and 0.51 cm^3 water per g of material, respectively.[21] On a per gram basis, UMON material has a lower sorption capacity (0.06 $cm^3\ g^{-1}$) due to the high atomic mass of uranium. However, on a per metal basis (mole H_2O per mole metal), the UMON material (2 : 1) falls within the range reported for the MOF materials (4 : 1 to 1 : 1).

Many water-stable MOF materials exhibit similar sorption isotherms, but variations exist due to specific structural components of the material. A majority of these MOFs sorb water when the relative humidity reaches 15 to 60%,[21] but some compounds (NH_3-MIL-53 (Al, Fe), HKUST, and CPO-27(MOF-74)) will immediately capture water upon exposure to the vapor phase.[49–51] Variations in water uptake is largely due to functionalization of the organic linkers and interactions with the metal nodes. Importance of the organic linker can be demonstrated by MIL-53, which contains the 1,4-benzenedicarboxylate molecule. The original form of this organic linker begins to sorb water when the relative humidity reaches 20%, but additional functionalization of the benzene ring to include a hydroxyl, carboxylate, or amine group drives immediate water uptake. It is hypothesized that these additional hydrophilic moieties can stimulate water uptake, and conversely, hydrophobic functional groups suppress the sorption process.[51] In HKUST and CPO-27(MOF-74), immediate water sorption is also observed upon exposure to the vapor phase, but the uptake mechanism differs in these materials. In these cases, it is the metal center that loses a ligated water molecule upon dehydration, resulting in a less-favored coordination geometry. The energetics of reinserting a water molecule into the first coordination shell of the metal drives the rapid uptake of water at low relative humidity levels.[49] These approaches to water sorption are driven by a substantial decrease in energy on sorption, but the disadvantage is that the dehydration process is also limited to very low relative humidity levels, which can lead to incomplete removal of the water from the material.

While exploring the literature on MOF sorption isotherms, we also noted that the solvent molecules in most of these materials experience significant disorder and the diffuse electron density cannot usually be modeled from the X-ray diffraction data. For instance, the crystalline lattice for MIL-53-ADP (Al) was determined using powder X-ray diffraction and Rietveld analysis.[52] However, the water within the nanopores cannot be characterized by this method, so the total water was determined by thermogravimetric analysis and the lattice positions were optimized by DFT calculations. Single crystal analysis of CPO-27-Zn provided information on the ligated water molecules and waters closely associated with the interior walls.[53] The remaining water molecules within the channel are so significantly disordered that the thermal displacement parameters range is between 0.348 to 0.297.

We previously demonstrated that the water molecules for the fully-hydrated UMON nanotubes are ordered, and similarly observe relatively well-ordered solvent for the partially hydrated materials. For this experiment, the UMON material was exposed to water vapor at 80% relative humidity for ten minutes, which resulted in a 1.51% weight gain for the sample. Structural analysis of the partially hydrated materials indicated the presence of two crystallographically unique water molecules (labeled OW1 and OW2) within the interior channels. These atoms were allowed to free refine, leading to occupancies of 22 and 19% for OW1 and OW2, respectively (Table 1). This indicates the presence of 0.41 moles of water per formula unit and a theoretical 1.26% weight increase, which agrees well with the 1.51% increase observed experimentally for the partially hydrated sample. For comparison, the structural characterization for the fully hydrated sample indicated full occupancy for both sites, although the electron density map of OW2 suggested that the high displacement parameter is associated with disorder of the site. The previously reported weight loss for the fully hydrated material (5.54%) also agrees with the theoretic value (5.6%), confirming the single-crystal X-ray diffraction analysis.

The similarity between the long-range ordering of the water molecules within the UMON compound and ice-like topology has not been previously reported for hybrid materials. As stated earlier, most water-stable MOF materials contain disordered or poorly ordered solvent molecules. While there are far fewer metal organic nanotubes reported in the literature, several other compounds also contain highly ordered solvent water molecules, including $[Cu(atc(H_2O)]\cdot H_2O$ (atc = 3-amino-1,2,4-triazole-5-carboxylate),[54] $[Zn(Imd)(Br)]\cdot H_2O$ (Imd = imidazolium diacetate),[55] and [Zn (ATIBDC)(bpy)]$\cdot 3H_2O$ (ATIBDC = 5-amino-2,4,6-triiodoisophtahlate).[56] The water molecules within these structures contain unique water clusters with up to 12 water molecules[54,56] as well as 1-D water wires,[55] but none of these compounds display ice-like topologies. This seems to be in contrast to MOF materials and could be related to the more confined nature of the pore space for nanotubular materials. Differences between the water ordering of metal organic nanotubes compared to metal organic frameworks is

Table 1 Refinement of the two crystallographically unique water molecules (OW1 and OW2) in the partial and fully hydrated UMON material

		x	*y*	*z*	U(eq.)	Occupancy
Partial hydration	OW1	0.0789(8)	0.1418(7)	1.461(3)	0.068(4)	0.22
	OW2	0.0858(11)	0.1629(11)	1.030(3)	0.079(5)	0.19
Full hydration[32]	OW1	0.0797(2)	0.1420(2)	−0.9646(7)	0.0489(11)	1.00
	OW2A	0.1105(8)	0.1655(8)	−0.540(2)	0.089(7)	0.50
	OW2B	0.0715(8)	0.1599(10)	−0.537(7)	0.094(6)	0.50

interesting, even with this small sample size, and suggests that 1-D confinement may enhance the ordered nature of the water molecules in these materials.

Turning back to the sorption isotherms, we can use the time dependent data to further model the kinetics of water capture for the UMON material. Kinetic and transport parameters found for the 45, 60 and 80% relative humidity data are provided in Table 2. Values of β between 0.1 and 10 are expected because this is the range where k and D/l^2 are comparable. The fit of equilibrium weight ($w_{eq.}$) (eqn (6)) provides β values of 3 to 4 for the range of relative humidity 45 to 80%. Summary is provided in Table 2 with more details in Fig. SI.10 to SI.12 and Tables SI.2 to SI.4. † Given β derived from equilibrium weight ($w_{eq.}$), the time dependent experimental data $w(t)$ are plotted as $w(t)$ *versus* log t and data overlaid on a plot of the model weight (sum $f(kt)$) *versus* log(kt) or log Dt/l^2. By shifting the axes to coincide, log k is found as log kt − log t = log k. Similarly, log Dt/l^2 − log D/l^2 = log to provide log D/l^2 (Fig. SI.10 to SI.12†). Fits are shown for average $w(t)$ in Fig. 3, which leads to average values for k and D/l^2 of $(3.7 \pm 1.5) \times 10^{-4}$ s^{-1} and $(2.9 \pm 1.5) \times 10^{-5}$ s^{-1}, respectively. The diffusion coefficient (D) can be calculated using the pore length (l) as equal to 2 μm to provide an average value of $(1.2 \pm 0.6) \times 10^{-12}$ cm^2 s^{-1}.

The diffusion coefficient associated with water sorption into the UMON compound is much lower than reported for other porous materials. Typical diffusion coefficients vary with the viscosity of the medium: in gas phase, D is of the order 0.1 cm^2 s^{-1}; in liquid water, 10^{-5} to 10^{-6} cm^2 s^{-1}; in solids, 10^{-10} to 10^{-12} cm^2 s^{-1}.[57] In nanostructured domains, diffusion can be impacted by tortuosity and limitations associated with similar sizes for the nanostructure and diffusing species. Zeolitic materials are stable in aqueous conditions and tend to exhibit measured, intrinsic diffusion coefficients on the order of 10^{-5} or 10^{-6} cm^2 s^{-1}.[58] Water sorption within single walled carbon nanotubes with diameters between 1 and 3 nm have been explored using both computational and experimental techniques and report values ranging between 10^{-5} to 10^{-6} cm^2 s^{-1}.[32,59–61] Given their relative instability in the presence of water, the values for water uptake in MOF materials have not been reported, but diffusion coefficients for other gaseous molecules including methane, ethane, CO_2, benzene, and hexane, range between 10^{-3} to 10^{-6} cm^2 s^{-1}.[62–65] The one exception is that of pyridine uptake into HKUST-1, where the diffusion coefficient was determined as 1.5×10^{-15} cm^2 s^{-1}.[66] In this case, the material does not simply sorb the pyridine molecule, but instead an exchange reaction takes place where a ligated water molecule on the Cu cation is removed *via* vacuum and then replaced with a pyridine molecule.[66] Diffusion of the pyridine molecule through the pore may be impeded upon ligation because the pore size for HKUST-1 is less than one nanometer and the shape is anisotropic (0.9 × 0.6 nm). Further, the reported diffusion coefficient may embed the rate of the kinetic processes, similar to the information characterized here by β. Where diffusion coefficients are measured without consideration of rate impacting chemical transformations, the diffusion coefficient may be underreported.

The diffusion coefficient for the UMON material, $(1.2 \pm 0.6) \times 10^{-12}$ cm^2 s^{-1}, is more comparable to values for some forms of bulk ice. Diffusion coefficients for water in vapor and in liquid water are faster at 0.28 cm^2 s^{-1} and 5×10^{-5} cm^2 s^{-1}, respectively. Diffusion of water molecules in bulk ice is 100 times slower (1.3×10^{-14} cm^2 s^{-1})[67] than that exhibited within the UMON material, whereas the rate calculated for low density amorphous (LDA) ice is quite similar (1×10^{-11} (170 K) to 2×10^{-14} (60 K) cm^2 s^{-1}).[68,69] LDA forms of ice are thermodynamically continuous with supercooled liquid water, where the deformation and diffusive behavior is viewed as more similar to viscous liquid than a solid ice.[69,70] LDA ice does show quasi-crystalline features that have similarities to hexagonal and cubic ice and is thought to be continuous with the icosahedral, expanded structure of the $(H_2O)_{280}$ water cluster.[71,72] In addition, ice-like structures can occur in filled carbon nanotubes at temperatures below 273 K, with diffusion coefficients of nanotubes with a diameter of 1.1 nm is 3×10^{-10} cm^2 s^{-1} and decreases to $<1 \times 10^{-10}$ cm^2 s^{-1} when the diameter increases to 2.0 nm.[32]

Similarities between LDA ice, ice-like arrays within carbon nanotubes, and the water within the UMON material is interesting because of the unique structural features of the confined water and the nature of the filling process. Filling the UMON nanotubes does not just involve simple sorption of gaseous

Table 2 Model fitting to β with equilibrium conditions ($w_{eq.}$)[a] for the UMON material at 45, 60, and 80% relative humidity (RH)

	45% RH	60% RH	80% RH	Average
$w_{eq.}/(2c^*\varepsilon l/r)$	0.47 ± 0.02	0.61 ± 0.02	0.47 ± 0.02	0.5 ± 0.1
β	4.1 ± 0.2	3.0 ± 0.1	4.1 ± 0.2	
Fit for β=	4	3	4	
log k	−3.7	−3.4	−3.3	
log D/l	−4.9	−4.37	−4.5	
k (s^{-1})	2.0×10^{-4}	4.0×10^{-4}	5.0×10^{-4}	$(3.7 \pm 1.5) \times 10^{-4}$
D/l^2 (s^{-1})	1.3×10^{-5}	4.3×10^{-5}	3.2×10^{-5}	$(2.9 \pm 1.5) \times 10^{-5}$
D (cm^2 s^{-1})	5.0×10^{-13}	1.7×10^{-12}	1.3×10^{-12}	$(1.2 \pm 0.6) \times 10^{-12}$
c^* (g cm^{-3})	1.04×10^{-5}	1.38×10^{-5}	1.84×10^{-5}	

[a] Equilibrium was measured at 90 minutes with the pore length (l) taken as 2 μm, and the porosity of 0.9732 for total access to internal volume (see ESI for additional details). For steady state at 166 min for 45% RH, a similar β of 3 (2.8 ± 0.6) is estimated.

molecules, but requires condensation of the water molecules into a hexameric motif that extends down the length of the nanotube. Based on the structural characterization of the UMON material, one crystallographically unique water molecule (OW1) maintains an ordered solid-like array even at room temperature, whereas the second water molecule (OW2) displays disorder even at 100 K.[33] These structural features combined with the calculated diffusion coefficient suggests an intermediate phase under nanoconfinement.

The diffusion within the UMON nanotubes are at least 100 times slower than the ice-like arrays found in carbon nanotubes and other metal organic materials, which could be associated with confinement effects or electrostatics within this system. MIL-53 is an interesting system that has been characterized by classical and quantum molecular dynamics simulations. When MIL-53 is either near total dehydration (0.5–1 H_2O per unit cell) or mostly hydrated (5–8 H_2O per unit cell) the pore space is approximately 1500 $Å^3$. Upon low water loading (1.5H_2O per unit cell) the material contracts to create a narrow pore configuration (950 $Å^3$).[73] Water molecules within the narrow pore configuration are restricted and exhibit lower transitional and rotational motion that have been attributed to nuclear quantum effects.[74,75] This leads to lower mobility compared to both the large pore configuration and bulk water. Computational assessment performed by Canepa *et al.* for CPO-27(MOF-74) also finds that slower diffusion for water over H_2 and CO_2 gases.[76] Based upon density functional theory calculations and *in situ* time resolved FTIR diffusion experiments, the mechanism responsible for molecular transport through the hydrated nanotube was related to simple longitudinal movement of the molecules. Fit of MIL-53 data to model (ESI; † eqn (5)) finds $\beta < 0.01$, consistent with diffusion controlled loading. The movement is suppressed more for H_2O compared to H_2 and CO_2 because of a larger calculated diffusion barrier (0.06 eV for H_2O compared to 0.005 eV for H_2).[76] From these previous studies, it seems like confinement of the water molecules within the UMON material can be related to the slower observed diffusion coefficients. However, a molecular dynamics study performed by Zhu and Schulten found that adding alternating positive and negative charge to the single-walled carbon nanotube also resulted in slower water diffusion within the tubes.[77] As the UMON nanotube contains a zwitterionic-like iminodiacetate ligand, this may also influence the water ordering and diffusion through the confined space.

From the model, the irreversible rate constant k is 4×10^{-4} s^{-1}. The frequency k measures the rate of irreversible loss from the gas phase. The nature of the irreversible reaction within the pore represent the rate at which the water in the pore condenses to the final structural state. According to the model and within the quality of the data fit, the condensation occurs by a first order, irreversible process. Unlike prior studies, the current model allows separation of transport (D) and kinetic (k) processes. β of 3 to 4 means transport and kinetics have comparable rates, which allows measurements under the experimental conditions. The observed rate constant for the UMON material is an order of magnitude lower than observed for single walled carbon nanotubes and porous activated carbon.[57,78] Subtle differences between the two forms of carbon suggested that the surface chemistry played a role in the uptake kinetics, whereby an increase in hydrophilic functional groups on the activated carbon decrease the rate of uptake. Similar effects could be taking place in the UMON material, where again the electrostatics of the ligand may influence the rate of water uptake.

Solvent uptake

Unlike other porous materials, UMON has previously been shown to be specific to liquid water over other liquid solvents; therefore, the selectivity of the material to gaseous vapors was also investigated using thermogravimetric analysis combined with FTIR analysis (Table 3). Samples were monitored by TGA for weight loss on heating; FTIR of outgassed material revealed only water was trapped in the channels; thus, the measurement does not discriminate for solvent sorbed on the particle surface. The sorbed water is reported as % uptake for the various solvents in Table 3 and the absolute uncertainty in these measurements is 0.5 to 0.7%. When the UMON sample was exposed to water, full uptake was observed, confirming the validity of the experimental design. In all cases, the evolved gas spectra indicated that water was the only solvent released as identified from the signature bands at 1300–2000 and 3500–3900 cm^{-1} (Fig. SI.18†) These data confirm that the UMON material is selective to water in the vapor phase, which again is

Table 3 Weight loss observed in the TGA and the properties of the solvents that was used for the analysis. FTIR of the released gases confirmed that the weight loss was the result of water uptake. No other solvents were observed within the UMON material

Solvent vapor	% uptake	Molar volume (cm^3 mol^{-1})	Solvent vapor	% uptake	Molar volume (cm^3 mol^{-1})
Methanol	1.25%	40.5	Benzene	1.17%	88.9
Ethanol	0.70%	58.4	Toluene	0.11%	106.3
1-Propanol	0.68%	74.8	Hexane	0.21%	131.6
1-Butanol	0.38%	91.5	Cyclohexane	0.08%	108.0
1-Pentanol	0.40%	108.3	Pentane	0.77%	115.3
2-Propanol	0.65%	112.3	Cyclopentane	0.06%	93.4
Acetone	0.60%	73.9			
THF	0.28%	81.4			
1,4-Dioxane	0.14%	85.3			
Water	5.50%	18.0			

not the case for other porous materials, such as CAU-10, MIL-53, MIL-101, or CPO-27.[21] Sorption of ammonia vapor was also explored because of the potential for hydrogen bonding, but exposure to the UMON material results in degradation of the crystalline phase. In Table 3, water uptake is noted with molar volume of the solvents, where the molar volume ($cm^3\ mol^{-1}$) for each solvent is calculated as molecular weight x (density)$^{-1}$. The general trend, at least for the water miscible solvents, is that water uptake increases as solvent molar volume decreases. Currently the chemical reasons for the exclusion of other solvents from the UMON material is unknown and further studies will focus on understanding the overall mechanisms for the observed selectivity.

Conclusions

Water sorption isotherms for the UMON material were collected and quantitatively evaluated. A diffusion coefficient (1×10^{-12} $cm^2\ s^{-1}$) and first order rate constant ($4 \times 10^{-4}\ s^{-1}$) characterize the water uptake process for relative humidity values from 45 to 80%. Full hydration was observed for relative humidity ≥60% and uptake completed within 75 minutes. Modeling the water sorption data led to a diffusion coefficient for the UMON material that is slower than in most porous materials and is most similar to that of amorphous ice. This result fits well with the ordered ice-like channel that exists in the hydrated UMON material even at room temperature. The first order irreversible rate constant may characterize the condensation from the vapor phase within the channel. Additional studies are ongoing to provide additional chemical understanding of this ordered array and how it changes with temperature.

Additional vapor sorption experiments indicated that the UMON material selectively sorbs water vapor and does not take up other common solvents. This level of selectivity is unusual for porous materials. Dehydrated UMON held in an environment saturated with solvent vapor for an extended period of time yields no evidence of solvent uptake, confirming exceptional and exclusive selectivity for water. The nanochannels are completely selective for water over many organic solvents, where the amount of water sorbed into the pore in the presence of solvent vapor tends to increase as solvent molar volume decreases. This selectivity remains one of the main advantages of the UMON materials over other porous solids and additional studies are necessary to understand the structural features of the material that lead to the extreme selectivity to water molecules for continued advancements in the area of water storage and separations.

Conflicts of interest

There are no conflicts to declare.

Acknowledgements

We acknowledge the NSF Division of Materials Research (DMR1252831) (TMZ; AJ, MP, DU, and AJ) and Division of Chemistry (CHE1309366) (JL) for funding this work.

References

1 N. K. Adam, *Nature*, 1948, **161**, 629–631.
2 P. G. Nilsson and B. Liindman, *J. Phys. Chem.*, 1983, **87**, 4756–4761.
3 R. Angelico, G. Palazzo, G. Colafemmina, P. A. Cirkel, M. Giustini and A. Ceglie, *J. Phys. Chem. B*, 1998, **102**, 2883–2889.
4 R. A. Day, B. H. Robinson, J. H. R. Clarke and J. V. Doherty, *J. Chem. Soc., Faraday Trans.*, 1979, **75**, 132–139.
5 S. Park, D. E. Moilanen and M. D. Fayer, *J. Phys. Chem. B*, 2008, **112**, 5279–5290.
6 I. Linossier, F. Galillard, M. Romand and J. F. Feller, *J. Appl. Polym. Sci.*, 1997, **66**, 2465–2473.
7 H. L. Yeager and A. Steck, *J. Electrochem. Soc.*, 1981, **128**, 1880–1884.
8 J. A. Barrie and B. Platt, *Polymer*, 1963, **4**, 303–313.
9 N. W. Ockwig, R. T. Cygan, L. Criscenti and T. M. Nenoff, *Phys. Chem. Chem. Phys.*, 2008, **10**, 800–807.
10 N. W. Ockwig, R. T. Cygan, M. A. Hartl, L. L. Daemen and T. M. Nenoff, *J. Phys. Chem. C*, 2008, **112**, 13629–13634.
11 S. D. Chemerisov and A. D. Trifunac, *Chem. Phys. Lett.*, 2001, 65–72.
12 N. W. Ockwig, J. A. Greathouse, J. Durkin, R. T. Cygan, L. L. Daemen and T. M. Nenoff, *J. Am. Chem. Soc.*, 2009, **131**, 8155–8162.
13 Y. Leng and P. T. Cummings, *Phys. Rev. Lett.*, 2005, **94**, 026101.
14 A. Delville, *J. Phys. Chem.*, 1993, **97**, 9703–9712.
15 U. Raviv, P. Laurat and J. Klein, *Nature*, 2001, **413**, 51–54.
16 E. Dujardin, T. W. Ebbesen, A. Krishnan and M. M. J. Treacy, *Adv. Mater.*, 1998, **10**, 1472–1475.
17 M. P. Rossi, Y. Gogotsi and K. G. Kornev, *Langmuir*, 2009, **25**, 2804–2810.
18 G. W. H. Wurpel and M. Muller, *Chem. Phys. Lett.*, 2006, **425**, 336–341.
19 Z. Arsov, M. Rappolt and J. Grdadolnik, *ChemPhysChem*, 2009, **10**, 1438–1441.
20 C. Castellano, J. Generosi, A. Congiu and R. Cantelli, *Appl. Phys. Lett.*, 2006, **89**, 233905.
21 J. Canivet, A. Fateeva, Y. Guo, C. Benoit and D. Farrusseng, *Chem. Soc. Rev.*, 2014, **43**, 5594–5617.
22 D. Ortiz-Young, H.-C. Chiu, S. Kim, K. Voitchovsky and E. Riedo, *Nat. Commun.*, 2013, **4**, 2–6.
23 M. A. Dokter, S. Woutersen and H. J. Bakker, *Phys. Rev. Lett.*, 2005, **94**, 178301.
24 E. Tombari, G. Salvetti and C. Ferrari, *J. Chem. Phys.*, 2005, **122**, 104712.
25 S. H. Garofalini, T. S. Mahadevan, S. Xu and G. W. Scherer, *ChemPhysChem*, 2008, **9**, 1997–2001.
26 N. Giovambattista, P. J. Rossky and P. G. Debenedetti, *Phys. Rev. Lett.*, 2009, **102**, 050603.
27 A. Alexiadis and S. Kassinos, *Chem. Rev.*, 2008, **108**, 5014–5034.
28 J. K. Holt, H. G. Park, Y. Wang, M. Stadermann, A. B. Artyukhin, C. P. Gringoerpoulos, A. Noy and O. Bakajin, *Science*, 2006, **312**, 1034–1037.

29 Z. Cao, Y. Peng, T. Yan, S. Li, A. Li and G. Voth, *J. Am. Chem. Soc.*, 2010, **132**, 11395–11397.
30 C. Dellago, M. M. Naor and G. Hummer, *Phys. Rev. Lett.*, 2003, **90**, 105902.
31 R. Renou, A. Szymczyk, G. Maurin, P. Malfreyt and A. Ghoufi, *J. Chem. Phys.*, 2015, **142**, 184706.
32 K. Koga, G. T. Gao, H. Tanaka and X. C. Zeng, *Nature*, 2001, **412**, 802–815.
33 D. K. Unruh, K. Gojdas, A. Libo and T. Z. Forbes, *J. Am. Chem. Soc.*, 2013, **135**, 7398–7401.
34 Y. Maniwa, H. Kataura, M. Abe, A. Udaka, S. Suzuki, Y. Achiba, H. Kira, K. Matsuda, H. Kadowaki and Y. Okabe, *Chem. Phys. Lett.*, 2005, **401**, 534–538.
35 A. S. Jayasinghe, S. Saltzman and T. Z. Forbes, *Cryst. Growth Des.*, 2016, **16**, 7058–7066.
36 C. A. Schneider, W. S. Rasband and K. W. Eliceiri, *Nat. Methods*, 2012, **9**, 671–675.
37 R. Hooft, *COLLECT*, Delft, The Netherlands, 1998.
38 G. M. Sheldrick, *APEX II*, Bruker AXS, Madison, WI, 1996.
39 G. M. Sheldrick, *SADABS*, University of Gottinger, Germany, 1996.
40 G. Sheldrick, *Acta Crystallogr., Sect. A: Found. Crystallogr.*, 2008, **64**, 112–122.
41 A. Jayasinghe, D. K. Unruh, A. Kral, A. Libo and T. Z. Forbes, *Cryst. Growth Des.*, 2015, **15**, 4062–4070.
42 P. Thanasekaran, T.-T. Suo, C.-H. Lee and K.-L. Lu, *J. Mater. Chem.*, 2011, **21**, 13140–13149.
43 S. L. James, *Chem. Soc. Rev.*, 2003, **32**, 276–288.
44 S. T. Meek, J. A. Greathouse and M. D. Allendorf, *Adv. Mater.*, 2011, **23**, 249–267.
45 D. Frohlich, E. Pantatosaki, P. D. Kolokathis, K. Markey, H. Reinsch, M. Baumgartner, M. A. van der Veen, D. E. De Vos, N. Stock, G. K. Papadopoulos, S. K. Henninger and C. Janiak, *J. Mater. Chem. A*, 2016, **4**, 11859–11869.
46 J. Arinez-Soriano, J. Albalad, C. Vila-Parrondo, J. Perez-Carvajal, S. Rodriguez-Hermida, A. Cabeza, J. Juanhuix, I. Imaz and D. Maspoch, *Chem. Commun.*, 2016, **52**, 7229–7232.
47 R. Plessius, R. Kromhout, A. L. Ramos, M. Ferbinteanu, M. C. Mittelmeijer-Hazeleger, R. Krishna, G. Rothenberg and S. Tanase, *Chemistry*, 2014, **20**, 7922–7925.
48 M. Wickenheisser, F. Jeremias, S. K. Henninger and C. Janiak, *Inorg. Chim. Acta*, 2013, **407**, 145–152.
49 J. Liu, Y. Wang, A. I. Benin, P. Jakubczak, R. R. Willis and M. D. LeVan, *Langmuir*, 2010, **26**, 14301–14307.
50 A. Shigematsu, T. Yamada and H. Kitagawa, *J. Am. Chem. Soc.*, 2011, **133**, 2034–2036.
51 H. Reinsche, M. A. van der Veen, B. Gil, B. Marszalek, T. Verbiest, D. de Vos and N. Stock, *Chem. Mater.*, 2012, **25**, 17–26.
52 H. Reinsche, R. S. Pillai, R. Siegel, J. Senker, A. Lieb, G. Maurin and N. Stock, *Dalton Trans.*, 2015, **45**, 4179–4186.
53 P. D. C. Dietzel, R. E. Johnsen, R. Blom and H. Fjellvag, *Chem.–Eur. J.*, 2008, **14**, 2389–2397.
54 T.-W. Tseng, T.-T. Luo and K.-H. Lu, *CrystEngComm*, 2014, **16**, 5516–5519.
55 Z. F. Fei, D. B. Zhao, T. J. Geldbach, R. Scopelliti, P. J. Dyson, S. Antonijevic and G. Bodenhausen, *Angew. Chem., Int. Ed.*, 2005, **44**, 5720–5725.
56 F. N. Dai, H. Y. He and D. F. Sun, *J. Am. Chem. Soc.*, 2008, **130**, 14064–14067.
57 E. Cussler and A. Varma, *Diffusion: Mass Transfer in Fluid Systems*, Cambridge University Press, Cambridge, 1997.
58 R. M. Barrer and B. E. F. Fender, *J. Phys. Chem. Solids*, 1961, **21**, 12–24.
59 Y. Liu and Q. Wang, *Phys. Rev. B*, 2005, **72**, 085420.
60 X. Liu, X. Pan, S. Zhang, X. Han and X. Bao, *Langmuir*, 2014, **30**, 8036–8045.
61 T. W. Allen, S. Kuyucak and S.-H. Chung, *J. Chem. Phys.*, 1999, **111**, 7985–7999.
62 F. Stallmach, S. Groger, V. Kunzel, J. Karger, O. M. Yaghi, M. Hesse and U. Muller, *Angew. Chem., Int. Ed.*, 2006, **45**, 2123–2126.
63 S. Amirjalayer, M. Tafipolsky and R. Schmid, *Angew. Chem., Int. Ed.*, 2007, **46**, 463–466.
64 H. Bux, C. Chmelik, R. Krishna and J. Caro, *J. Membr. Sci.*, 2011, **369**, 284–289.
65 N. Rosenbach, H. Jobic, A. Ghoufi, F. Salles, G. Maurin, S. Bourrelly, P. L. Llewellyn, T. Devic, C. Serre and G. Ferey, *Angew. Chem., Int. Ed.*, 2008, **47**, 6611–6615.
66 O. Zybaylo, O. Shekhah, H. Wang, M. Tafipolsky, R. Schmid, D. Johannsmann and C. Woll, *Phys. Chem. Chem. Phys.*, 2010, **12**, 8092–8097.
67 V. F. Petrenko and R. W. Whitworth, *Physics of Ice*, Oxford University Press, Oxford, 1999.
68 P. Ghesquiere, T. Mineva, D. Talbi, P. Theule, J. A. Noble and T. Chiavassa, *Phys. Chem. Chem. Phys.*, 2015, **17**, 11455–11468.
69 R. S. Smith, Z. Dohnalek, G. A. Kimmel, K. P. Stevenson and B. D. Kay, *Chem. Phys.*, 2000, **258**, 291–305.
70 O. Mishima and H. E. Stanley, *Nature*, 1998, **396**, 329–335.
71 J. Urquidi, C. J. Benmore, P. A. Egelstaff, M. Guthrie, S. E. Mclain, C. A. Tulk, D. D. Klug and J. F. C. Turner, *Mol. Phys.*, 2004, **102**, 2007–2014.
72 O. Loboda and V. Goncharuk, *Chem. Phys. Lett.*, 2010, **484**, 144–147.
73 F. Salles, s. Bourrelly, H. Jobic, T. Devic, V. Guillerm, P. Llewellyn, C. Serre, G. Ferey and G. Maurin, *J. Phys. Chem. C*, 2011, **115**, 10764–10776.
74 G. R. Medders and F. Paesani, *J. Phys. Chem. Lett.*, 2014, **5**, 2897–2902.
75 F. Paesani, *Mol. Simulat.*, 2012, **38**, 631–641.
76 P. Canepa, N. Nijem, Y. J. Chabal and T. Thonhauser, *Phys. Rev. Lett.*, 2013, **110**, 026102.
77 F. Zhu and K. Schulten, *Biophys. J.*, 2003, **85**, 236–244.
78 P. Kim, Y. Zheng and S. Agnihotri, *Ind. Eng. Chem. Res.*, 2008, **47**, 3170–3178.